Control Engineering Practice 43 (2015) 94–108

Contents lists available at ScienceDirect

Control Engineering Practice

journal homepage: www.elsevier.com/locate/conengprac

Robustness analysis of a PI controller for a hydraulic actuator

Lisandro J. Puglisi [a,*,1], Roque J. Saltaren [a], Cecilia Garcia [a], Ilka A. Banfield [b,2]

[a] Centro de Automática y Robótica, Universidad Politécnica de Madrid – CSIC, C. José Gutierrez de Abascal, 6, 28006 Madrid, Spain
[b] Universidad Tecnológica de Panamá, Campus Victor Levi Sasso, Panamá, Panama

ARTICLE INFO

Article history:
Received 22 December 2013
Received in revised form
28 June 2015
Accepted 28 June 2015
Available online 24 July 2015

Keywords:
Servo-hydraulic actuator
PI controller
Robustness
Small gain theorem

ABSTRACT

In this work the authors address the problem of robustness of the classic PI controller implemented in a Hydraulic Servo-Actuator (HSA), by presenting a strategy based on the definition of a linear model of the system and the identification of its parameters for different working points. The variation of these parameters is considered as a measure of parametric uncertainty of the linear model. These uncertainties along with the definition of a nominal plant are used to analyze the robustness of the system implementing the Small Gain Theorem. Theoretical and experimental results show that a PI controller can provide robustness to the HSA.

1. Introduction

The dynamics of hydraulic systems are highly nonlinear due to the physical properties present in the system such as fluid compressibility, pressure losses, transient and turbulent flow conditions and non-linear friction characteristics in the hydraulic actuator.

These nonlinear characteristics demand the development of advanced control strategies when high performance response is required (Bobrow & Lum, 1995; Chen, Renn, & Su, 2005; Hwang, 1996; Kim & Tsao, 2000; Mohanty & Yao, 2011; Zhao & Virvalo, 1995; Zulfatman & Rahmat, 2009). Even though the nonlinear characteristics of the system cannot be neglected, attempts are also found in the literature to develop control strategies based on linear models of the HSA (Karpenko & Sepehri, 2005; Kim, 1997; Kim & Tsao, 2000; La Hera et al., 2008; Laval, 1996; Niksefat & Sepehri, 2001; Rahmat, Rozali, Wahab, Zulfatman, & Kamaruzaman, 2010).

Depending on the consideration taken, the simplified linear models have the general form of a third (Jelali & Kroll, 2002) or fourth order (Watton, 1989) type-I system. Nevertheless, in both models it can be distinguished two parts: one associated to the control input and the other associated to the effect of external forces. In general, for the design of the controller the latter one is discarded and only the first part is considered (Sepehri, Corbet, & Lawrence, 1995).

In this work, it is demonstrated that the later assumption leads to non-zero steady state error with classic P-controller, and that it is necessary to appeal to a PI-controller. However, it is controversial to use a PI controller with a type-I system, since the open loop system will have two poles at the origin and thus reducing the stability of the closed loop.

In this work the robustness of a HSA with a classic PI controller is assessed.

The approach presented in this work implements the linearized model of the system presented in Jelali and Kroll (2002), whose parameters are experimentally identified for different working points of the system (i.e. different positions and external load conditions). The variability of these parameters is considered as a measure of parametric uncertainties present in the linear model and is used to provide boundaries that will define the robustness of the system in terms of its stability and insensibility to external perturbations using the Small Gain theorem.

The main contributions of this work are the following:

- P-controller cannot provide zero steady state error, and it can only be achieved with a PI-controller.
- Classical PI controller can provide robustness to the HSA.
- Classical PD and PID controllers may lead to instability issues.

The rest of this work is organized as follows. Firstly, the linearized model of the HSA is derived and analyzed. Then, the experimental identification procedure of the system is completely

* Corresponding author.
E-mail addresses: lisandro.puglisi@alumnos.upm.es (L.J. Puglisi), rsaltaren@etsii.upm.es (R.J. Saltaren), cecilia.garcia@upm.es (C. Garcia), ilka.banfield@utp.ac.pa (I.A. Banfield).

[1] MAEC-AECID grant programs.
[2] Secretaría Nacional de Ciencia y Tecnología de Panamá Becas de Excelencia grant programs.

http://dx.doi.org/10.1016/j.conengprac.2015.06.010
0967-0661/

Nomenclature

P_L	load pressure
P_A, P_B	pressure at chambers A and B
Q_A, Q_B	oil flow through control Port A and Port B
α	ratio of the effective surfaces at both sides of the piston
A_p	effective surface of the piston
c_{vi}	discharge coefficient of the orifices
x_v	servo-valve's input signal and servo-valve's spool position
K_{xA}, K_{xB}	flow sensibility constant regarding the spool position
K_{P_A}, K_{P_B}	flow sensibility constant regarding the pressure at the cylinder chambers
V_{A0}, V_{B0}	initial volume at the chambers
m	total mass. It consists of the piston mass, the mass of hydraulic fluid in the cylinder chambers and the external load
β_A and β_B	bulk modulus of the fluid at chambers A and B of the cylinder

detailed and 33 sets of parameters and their corresponding transfer functions are found. From the experimental identification a nominal plant is defined and some considerations regarding the stability and steady state error with classical P, PI, PD and PID controllers are presented. Following this, the robustness of the system is analyzed implementing the Small Gain Theorem. The real HSA is submitted to several experiments in order to prove the performance of the PI controller and finally, the conclusions and discussions are stated.

2. Theoretical model of HSA

The complete model of a HSA derives from complex equations that depend on many parameters that cannot be always accurately obtained and the rigorousness of the model is lost. However, considering that the dynamics of the system are governed by the slower dynamics (i.e. the dynamics of the piston), some of the dynamics derived from the internal components of the servo-valve can be neglected (Jelali & Kroll, 2002; Watton, 1989). It is a common practice to simplify the system into the orifice equation for the servo-valve, the pressure dynamics at the cylinder, and the dynamic equation of motion.

In particular for the linearized model, the latter equations are expressed in terms of the load pressure given by $P_L = P_A - \alpha P_B$, and it is considered that the flow through the orifices is in a steady state, i.e. $Q_A = A_p\dot{y}$ and $Q_B = \alpha A_p\dot{y}$.

Taking an operating point $\boldsymbol{P_0} = [x_{v0},\ P_{A0},\ P_{B0}]$, and assuming dominance of the first order term from the Taylor series expansion, the set of linearized equations are stated as follows.

Linearized pressure equation:

$$\delta P_A = \begin{cases} \dfrac{R_{h1}}{R_{h1} + \alpha^3 R_{h4}}\delta P_L & \text{for } x_v \geq 0 \quad \text{(a)} \\ \dfrac{R_{h2}}{R_{h2} + \alpha^3 R_{h3}}\delta P_L & \text{for } x_v < 0 \quad \text{(b)} \end{cases} \tag{1}$$

$$\delta P_B = \begin{cases} -\dfrac{\alpha^2 R_{h4}}{R_{h1} + \alpha^3 R_{h4}}\delta P_L & \text{for } x_v \geq 0 \quad \text{(a)} \\ -\dfrac{\alpha^2 R_{h3}}{R_{h2} + \alpha^3 R_{h3}}\delta P_L & \text{for } x_v < 0 \quad \text{(b)} \end{cases} \tag{2}$$

where $R_{hi} = 1/(x_v c_{vi})^2$.

Linearized orifice equation for the servo-valve:

$$\delta Q_A = K_{x_A}\delta x_v + K_{P_A}\delta P_A, \tag{3}$$

$$\delta Q_B = K_{x_B}\delta x_v + K_{P_B}\delta P_B. \tag{4}$$

Linearized pressure dynamics: Adopting that fluid flows into chamber A and flows out of chamber B while the pistons's rod extends with positive velocity (see Fig. 1), then

$$\delta Q_A = A_p\delta\dot{y} + \frac{V_{A0}}{\beta}\frac{d}{dt}[\delta P_A], \tag{5}$$

$$\delta Q_B = \alpha A_p\delta\dot{y} - \frac{V_{B0}}{\beta}\frac{d}{dt}[\delta P_B]. \tag{6}$$

Linearized equation of motion: In order to simplify the model, it is considered that the friction is governed by the classic *static+viscous* friction model given by $F_f(y) = F_s + \sigma\dot{y}$, where F_s is the static friction coefficient and σ is the viscous friction coefficient. Therefore, the linearized equation of motion is given by

$$A_p(\delta P_A - \alpha\delta P_B) - \delta F_{ext} - \delta F_f = m\delta\ddot{y}. \tag{7}$$

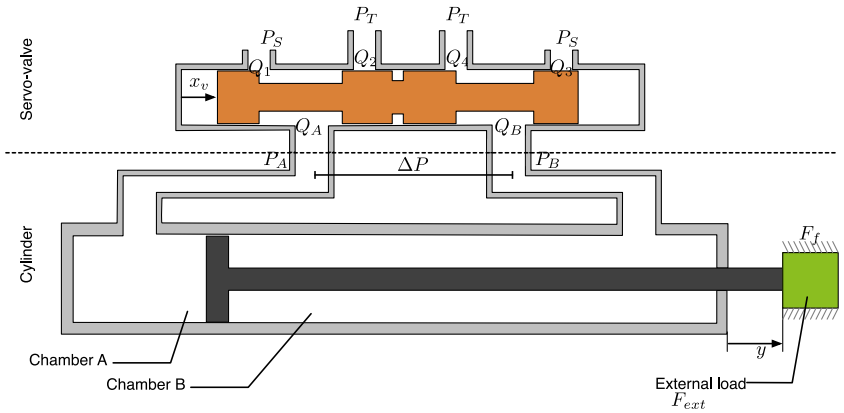

Fig. 1. Schematic diagram of the simplified SHA.

Recalling that the time derivative of the load pressure is given by $\dot{P}_L = \dot{P}_A - \alpha\dot{P}_B$, and combining the linearized expressions, the load pressure dynamic can be expressed in terms of the servo-valve sensibility constants as follows:

$$\delta\dot{P}_L = K_x\delta x_v - K_d\delta\dot{y} + K_p\delta P_L \tag{8}$$

where

$$K_x = \frac{\beta_A}{V_A}K_{xA} + \alpha\frac{\beta_B}{V_B}K_{xB} \tag{9}$$

$$K_d = A_p\left(\frac{\beta_A}{V_A} + \alpha^2\frac{\beta_B}{V_B}\right) \tag{10}$$

$$K_p = \frac{\beta_A}{V_A}K_{PA}R_i - \alpha\frac{\beta_B}{V_B}K_{PB}R_j \tag{11}$$

and

$$R_i = \begin{cases} \dfrac{R_{h1}}{R_{h1} + \alpha^3 R_{h4}} & \text{for } x_v \geq 0 \quad \text{(a)} \\ \dfrac{R_{h2}}{R_{h2} + \alpha^3 R_{h3}} & \text{for } x_v < 0 \quad \text{(b)} \end{cases} \tag{12}$$

$$R_j = \begin{cases} -\dfrac{\alpha^2 R_{h4}}{R_{h1} + \alpha^3 R_{h4}} & \text{for } x_v \geq 0 \quad \text{(a)} \\ -\dfrac{\alpha^2 R_{h3}}{R_{h2} + \alpha^3 R_{h3}} & \text{for } x_v < 0 \quad \text{(b)} \end{cases} \tag{13}$$

Therefore, based on (7) and (8) and defining the state variables: $x_1 = \delta y$, $x_2 = \delta\dot{y}$, $x_3 = \delta P_L$, and the input variables: $u_1 = \delta x_v$, $u_2 = \delta F_e$, the governing dynamics of the HSA can be stated as

$$\begin{bmatrix} \dot{x}_1 \\ \dot{x}_2 \\ \dot{x}_3 \end{bmatrix} = \begin{bmatrix} 1 & 0 & 0 \\ 0 & -\dfrac{\sigma}{m} & \dfrac{A_p}{m} \\ 0 & -K_d & K_p \end{bmatrix}\begin{bmatrix} x_1 \\ x_2 \\ x_3 \end{bmatrix} + \begin{bmatrix} 0 \\ 0 \\ K_x \end{bmatrix}u_1 + \begin{bmatrix} 0 \\ -\dfrac{1}{m} \\ 0 \end{bmatrix}u_2. \tag{14}$$

2.1. Model analysis

Applying the Laplace transform (i.e. $\mathcal{L}(\cdot)$) to (7) and (8), it is obtained as follows:

$$s\Delta P_L = K_x\Delta X - K_d\Delta V + K_p\Delta P_L, \tag{15}$$

$$A_p\Delta P_L = ms\Delta V + \sigma\Delta V + \Delta F_e, \tag{16}$$

where $\Delta X(s) = \mathcal{L}\{x_v(t)\}$, $\Delta P_L(s) = \mathcal{L}\{\delta P_L(t)\}$, $\Delta F_e(s) = \mathcal{L}\{\delta F_e(t)\}$, $\Delta V(s) = \mathcal{L}\{\delta\dot{y}(t)\}$. Solving (15) for ΔPL, and replacing it in (16), the governing dynamics of the system can be expressed as follows (Rahmat et al., 2010):

$$\Delta V = \frac{A_pK_x}{s^2b_2 + sb_1 + b_0}\Delta X - \frac{s - K_p}{s^2b_2 + sb_1 + b_0}\Delta F_e \tag{17}$$

where $b_2 = m$, $b_1 = -mK_p + \sigma$, and $b_0 = A_pK_d - \sigma K_p$.

Regarding that $\Delta V = \frac{1}{s}\Delta Y$, and expressing the denominator in the canonical form $s(s^2 + 2\zeta w_n s + w_n^2)$, (17) can be rearranged as

$$\Delta Y = \frac{k_{01}\,b_0'}{s(s^2 + b_1's + b_0')}\Delta X - \frac{k_{02}\,b_0'(s + z_0)}{s(s^2 + b_1's + b_0')}\Delta F_e, \tag{18}$$

where

$$b_1' = -K_p + \frac{\sigma}{m}, \tag{19}$$

$$b_0' = \frac{A_pK_d - \sigma K_p}{m}, \tag{20}$$

$$k_{01} = \frac{A_pK_x}{mb_0'}, \tag{21}$$

$$z_0 = -K_p, \tag{22}$$

$$k_{02} = \frac{1}{mb_0'}. \tag{23}$$

From (18), it can be seen that the piston position (ΔY) depends not only on the input signal of the servo-valve (ΔX) but also on the external perturbations (ΔF_e).

For a first analysis, let us assume that there is no external perturbation (i.e. $\Delta F_e = 0$), and let us define the transfer function $G(s) = \Delta Y(s)/\Delta X(s)$. This reduced system $G(s)$ posses a pole at the origin, revealing the integrating behavior of the system, i.e. a constant input ΔX, after its transient response produces a displacement at constant velocity. The two other poles form a conjugate complex pole pair (Jelali & Kroll, 2002), and they define most of the system's dynamics. The natural frequency w_n and damping ζ of these pair of poles are given by (24) and (25) respectively

$$w_n = \sqrt{\frac{K_dA_p - \sigma K_p}{m}}, \tag{24}$$

$$\zeta = \frac{\sigma - mK_p}{2\sqrt{m(K_dA_p - \sigma K_p)}}. \tag{25}$$

From these expressions, it can be seen that the natural frequency depends on the mass (m) and the stiffness of the cylinder's chamber (K_d and K_p). The latter one is position dependent. Therefore, for a given position, the location of the complex pole pair tends to the origin of the complex plane ($\mathbb{C}$) as m increases. On the other hand, the damping is governed by the viscous friction σ/m.

With regard to the stability of $G(s)$ and according to Routh–Hurtwitz criteria, b_1' and b_0' should be positive and non-zero. Thus, the following inequalities should be met:

$$K_p < \frac{\sigma}{m}, \tag{26}$$

$$K_d > \frac{\sigma K_p}{A_p}. \tag{27}$$

By definition $\sigma > 0$ and $m > 0$, therefore $K_p < 0$. This result can also be observed in (10), where it can be easily demonstrated that $K_{PA} < 0$ and $K_{PB} < 0$. Thus, based on this consideration, and assuming that $A_p > 0$, from (27) it is found that K_d is positive.

Considering the complete model (18) once again, it is seen in (22) that the current zero (z_0) depends of the flow pressure coefficients (see (22)), and it is located on the left half plane ($\mathbb{C}^-$) of the complex plane ($\mathbb{C}$). Even more, the location of this zero is placed at the left of the complex pole pair, since the real part of the complex pole pair ($\mathrm{Re}(p_i)$) is given by

$$\mathrm{Re}(p_i) = \zeta w_n = \frac{1}{2}\left(K_p + \frac{\sigma}{m}\right), \tag{28}$$

therefore $\mathrm{Re}(p_i) > z_0$.

These results are helpful for the identification process.

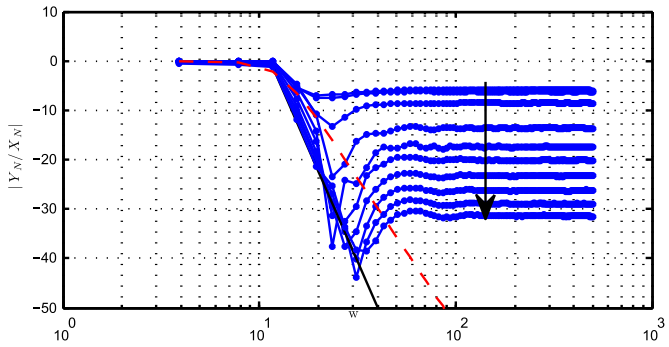

Fig. 2. Empirical transfer function estimation for the SHA in close loop. (For interpretation of the references to color in this figure caption, the reader is referred to the web version of this paper.)

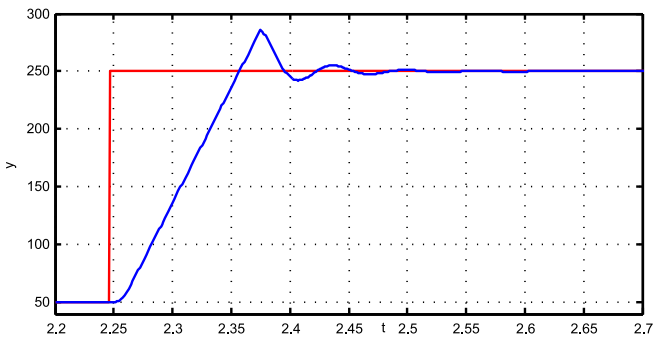

Fig. 3. Velocity constraint limitation. (For interpretation of the references to color in this figure caption, the reader is referred to the web version of this paper.)

2.2. Experimental verification of the linearized model

Despite the fact that the linearized model presented in the previous section is well known, it can be of major use to verify whether this model may provide the dynamics of the real system and analyze its limits.

A first approach would be to analyze the frequency response of the system and compare it with the structure of the linearized model.

This can be done by submitting the SHA to PRBS input signals and then implementing an empirical transfer function estimation (ETFE) by correlating the input/output data. However, as it was mentioned previously, the linearized model is obtained by linearizing the main dynamics of the system around a defined working point, i.e. a defined position with a defined external load. Given the nature of the SHA, this can only be done in closed loop with a position controller.

In Fig. 2 is presented in blue the ETFE of the system for different PRBS amplitudes. As it can be seen in this figure, for the low frequency the ETFE is plane and it presents a cut-off frequency approximately at 10 rad/s. After the cut-off frequency the estimated frequency response decays asymptotically and it reaches its minimum in the 20–30 rad/s frequency band.

The dashed red line represents the frequency response of a generic third order system with $w_n=10$ and $\zeta=0.5$ defined in expression (29), resulting from the close loop transfer function of $G(s)$ with a proportional controller

$$G_{cl}(s) = \frac{K}{(s + w_n)(s^2 + 2\zeta w_n s + w_n^2)} \tag{29}$$

The black arrow indicates the frequency response for increasing amplitude of the PRBS input signal. For this analysis, it was considered amplitudes of 5, 10, 25, 50, 75, 100, 125, 150, 175 and 200 mm.

As it can be seen, the inclination of the asymptotic increases with the amplitude of the PRBS input signal. This means that the order of the system increases, which reveals that the model is no longer linear for such spanning. The asymptotic with the biggest inclination was obtained for an amplitude of 200 mm in the input signal, and its inclination was approximately -170 dB/dec requiring a higher order system (depicted as black line in Fig. 2). For amplitudes up to 50 mm in the input signal the asymptotic presents an inclination of -60 dB/dec, which is in line with the linearized model.

The requirements of higher order system for bigger input amplitudes are related with the fact that the velocity of the SHA is limited by the maximum flow that the hydraulic power station can deliver. The effect of this limitation can be appreciated in Fig. 3, where the output position of the SHA (blue curve) presents a triangular response during the first 150 ms for a 200 mm input signal (red curve).

3. Experimental identification

The identification process consists of exciting the real system with a proper input signal in order to capture as much dynamics in its outputs, and adjust the parameters of the proposed model so that it can emulate the real system as much as possible (Ljung, 2002). There is no-unique methodology to perform this task (see Jelali & Schwarz, 1995; Liao, Roelle, Chen, Park, & Gerdes, 2011; Liu & Daley, 1999; Ling, Rahmat, Husain, & Ghazali, 2011; Rahmat et al., 2010). Indeed, it is an iterative process that requires common sense and intuition and it depends on the expertise of the performer to get to the most appropriate results.

3.1. Identification process

The identification methodology implemented in this work is composed of three main iterative steps (see Fig. 4):

1. *Experimentation*: This is perhaps the most critical step during the identification process, since it requires the definition of an experiment from whom the system's dynamics could be extracted. The experiment is detailed in Section 3.1.1.
2. *First ID*: In this step a first identification of some parameters is carried on. As it is depicted in Fig. 4, two different sets of parameters are identified. The first set of parameters are related to the piston's motion dynamics (i.e. the total mass, the viscous friction and external perturbation: m, σ, and F_e, respectively). The second set of parameters corresponds to the open-loop transfer function $G(s)$ that relates to the input–output data. These two identifications are performed in parallel in order to reduce the error estimation.
3. *Accuracy improvement*: The sensibility constants (K_p, K_d and K_x) are calculated from the identified motion's dynamics parameters and the open loop transfer function. The linearized model is generated and then validated. K_p, K_d and K_x are modified in order to maximize the accuracy.

3.1.1. Experimental design

The parameters of the linearized model found depend both on the piston's position and the pressure at the cylinder's chambers. Thus, the system has to be identified for several positions and pressures. Since the HSA in the open loop is a velocity system (i.e. for a constant input the HSA provides a movement with constant velocity), in order to achieve a desired position the experimental identification must be performed in a closed loop with a position

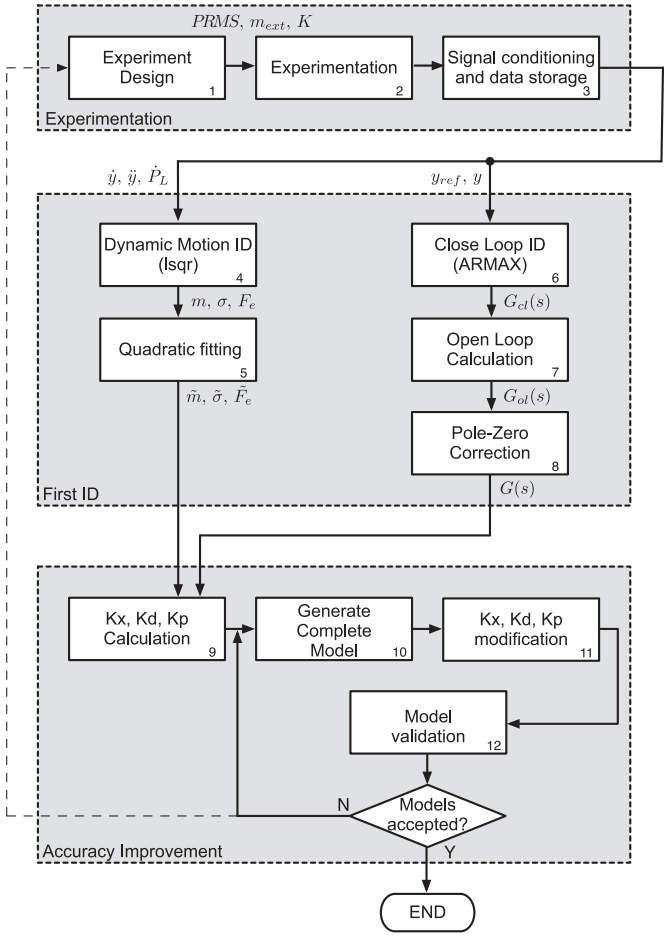

Fig. 4. Identification process.

controller. For identification purposes, a proportional controller is more than adequate.

On the other hand, for non-linear systems it is important to capture as much dynamics as possible therefore

- the proportional term must be chosen to obtain an underdamped response.
- all the amplitudes and frequencies and all their combinations must be represented in the input signal. Thus, a Pseudo-Random Multilevel Signal (*PRMS*) is implemented since they provide an excitation with random level at random instances, taking special attention that the output response does not exceed certain limits in order to be consistent with the linearization concept.

In order to provide different pressure points, the experiments are performed for several external loads.

During the experimentation, the supply pressure (P_s) is set to 25 bar, and the following variables are registered:

- y_{ref}: *PRMS* signal.
- x_v: input signal of servo-valve.
- P_A and P_B: pressure at the piston's chambers A and B, respectively.
- y: piston's position.

The signals captured with analog sensors (i.e. P_A, P_B) are filtered with a fourth-order Butterworth low-pass filter with $f_c = 400$ Hz.

3.1.2. Closed loop transfer function identification

For the first step of the identification process, it is assumed that the open loop system is given by the following third order type-I system:

$$G(s) = \frac{numG(s)}{denG(s)} = \frac{kw_n^2}{s(s^2 + 2\zeta w_n + w_n^2)}, \tag{30}$$

therefore, the input–output behavior in close loop will be given by

$$G_{cl}(s) = \frac{KG(s)}{1 + KG(s)} = \frac{KnumG(s)}{denG(s) + KnumG(s)}. \tag{31}$$

For all the input–output data (i.e. y_{ref} and y) from the experiment, a third order model is determined implementing an ARMAX structure from the identification toolbox of Matlab® (Ljung, 2002). The identified models correspond to the close-loop system $G_{cl}(s)$. However, since the proportional controller K is known, the open loop transfer function can be found as follows:

$$G_{ol}(s) = \frac{1}{K}\frac{numG_{cl}(s)}{denG_{cl}(s) - numG_{cl}(s)} \tag{32}$$

As it is common with models with poles at the origin, the identified models may present additional zeros and poles. Therefore, this inaccuracy must be corrected by selecting the poles and zeros that govern the dynamics. The new corrected model $G(s)$ is again validated with the experimental data.

3.2. Dynamic motion parameters identification

Based on the linearized expression:

$$A_p\delta P_L = m\delta\ddot{y} + \sigma\delta\dot{y} + \delta F_e, \tag{33}$$

a linear system $\boldsymbol{A}(t)\boldsymbol{\theta}(t) = \boldsymbol{B}(t)$ is defined as

$$\begin{bmatrix} \ddot{y}(1) & \dot{y}(1) & 1 \\ \ddot{y}(2) & \dot{y}(1) & 1 \\ \vdots & \vdots & \vdots \\ \ddot{y}(n) & \dot{y}(n) & 1 \end{bmatrix} \begin{bmatrix} m \\ \sigma \\ F_e \end{bmatrix} = \begin{bmatrix} A_pP_L(1) \\ A_pP_L(2) \\ \vdots \\ A_pP_L(n) \end{bmatrix}. \tag{34}$$

and it is solved by implementing the least squares method provided with the *lsqr* function of Matlab®. The parameters obtained are fitted to a second order polynomial dependent on the position, i.e. $\tilde{m}(y)$, $\tilde{\sigma}(y)$, $\delta\tilde{F}_e(y)$.

3.2.1. Sensibilities constants improvement

From (19) to (21) and using the parameters found of $G(s)$ and $\tilde{m}(y)$, $\tilde{\sigma}(y)$, $\delta\tilde{F}_e(y)$, the sensibility constants can be found as follows:

$$K_p = -b_1' + \frac{\tilde{\sigma}}{\tilde{m}}, \tag{35}$$

$$K_d = \frac{1}{A_p}(\tilde{m}b_0' + \tilde{\sigma}K_p), \tag{36}$$

$$K_x = \frac{1}{A_p}(\tilde{m}b_0'k_{01}). \tag{37}$$

The complete linearized model is generated as follows:

$$Y = \frac{k_{01}b_0'}{s(s^2 + b_1's + b_0')}X_v - \frac{k_{02}b_0'(s + z_0)}{s(s^2 + b_1's + b_0')}F_e. \tag{38}$$

Using the input–output data of the experiment, the sensibility constants K_x, K_d and K_p are modified in order to maximize the accuracy of the model, defining the following fitting index:

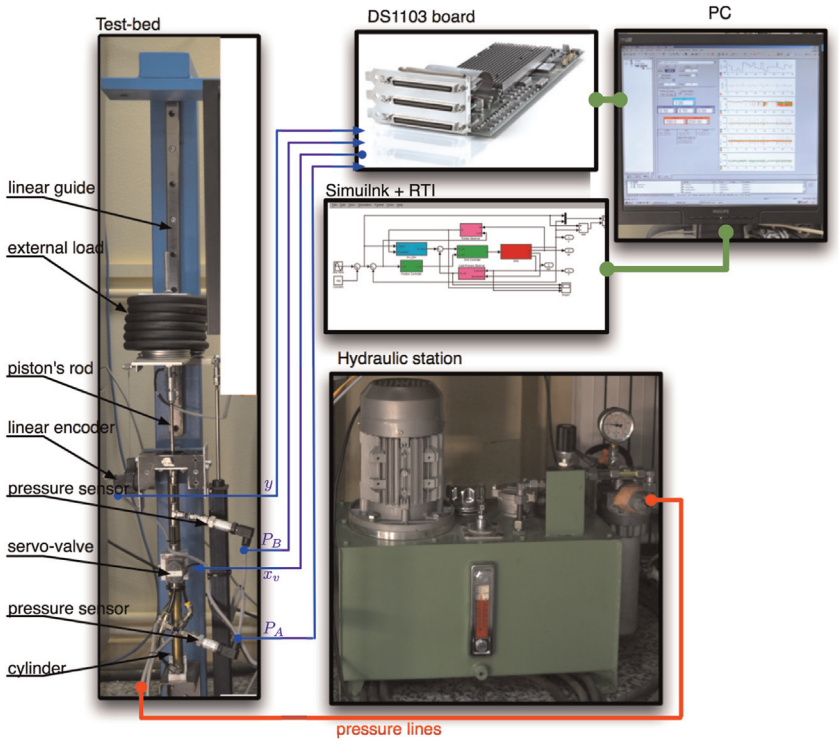

Fig. 5. Experimental setup.

$$F = 1 - \frac{\|(y - y_s)\|}{\|(y - \overline{y})\|}, \tag{39}$$

where y is the output data from the experiment, and y_s is the simulated output data with the transfer function (38).

3.3. Hydraulic actuator and experimental setup

The main elements of the HA are the double-effect cylinder CylVal 300-series (304 mm of maximum stroke) and the Moog E050 miniature servo-valve (double stage, closed-center, 6,9 L/min flow-rate, 350 Hz bandwidth). The HA is powered by a gear pump driven by a 1HP electric motor capable of delivering 10 L/min flow rate at 40 bar. For this work the power station was set to 5 L/min at 25 bar approximately.

The experimental setup is basically composed of a steel structure anchored at the floor with a stainless steel linear guide. The cylinder is attached to the structure and the cylinder rod is coupled to the sliding element of the linear guide in order to provide a linear movement (see Fig. 5).

Two pressure sensors are placed between the output ports of the servo-valve and the input ports of the cylinder, providing the pressure from the respective cylinder's chambers.

A dSPACE DS1103 board is implemented as the control hardware. It captures data from the pressure sensors (P_A and P_B) and linear encoder (y), and it also provides the control signal (x_v) to the servo-valve.

The experiment is fully designed in Simulink® and embedded in the controller board with the Real-Time Interface (RTI). An interface developed with the dSPACE ControlDesk® provides real time full control on the experiment and data visualization.

3.4. Experimental identification

3.4.1. Experiment #1: PRMS response under closed loop

Objective: Finding the parameters that characterizes the behavior of the hydraulic actuator for each set point and external load.

Description: The HSA is submitted to *PRMS* input signals in closed loop, driving external loads of 0, 3 and 6 kg. A proportional position controller is implemented. The range of displacement of the HSA is divided into 11 positions, separated by 30 mm, except for the first and the last set-point that are defined at 10 mm and 290 mm respectively. The *PRMS* provides a centered signal with random amplitude and random width. Its amplitude ranges within $\pm$ 10 mm and its width ranges from 1 s to 6 s. Registers of 50 s are obtained. For each position and load, five different *PRMS* signals are used, with different proportional controllers.

Data processing: For the first ID step, it is only considered the transient response of the system. Therefore, each change in the *PRMS* signal is detected and a window of 150 ms is used for the identification. δP_L is calculated from P_A and P_B, as follows: $\delta P_L = P_A - \alpha P_B$. $\dot{y}$ and $\ddot{y}$ are obtained implementing finite difference on y, and a fourth order Butterworth low-pass filter with a cut off frequency of 200 Hz.

Results: In Fig. 6 presented in red is a typical *PRMS* signal used during the experimental identification and the position response of the system in blue. The curves correspond to an experiment for a set point of 10 mm with non-external load (i.e. 0 kg). As it can be

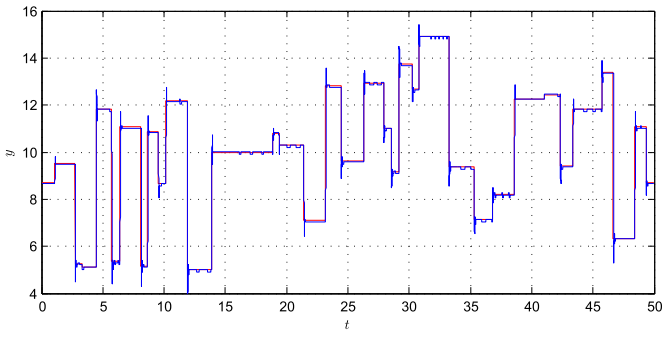

Fig. 6. Input–output experimental data. *PRMS* input signal (i.e. u_{ref}) in red, pistons response in blue. (For interpretation of the references to color in this figure caption, the reader is referred to the web version of this paper.)

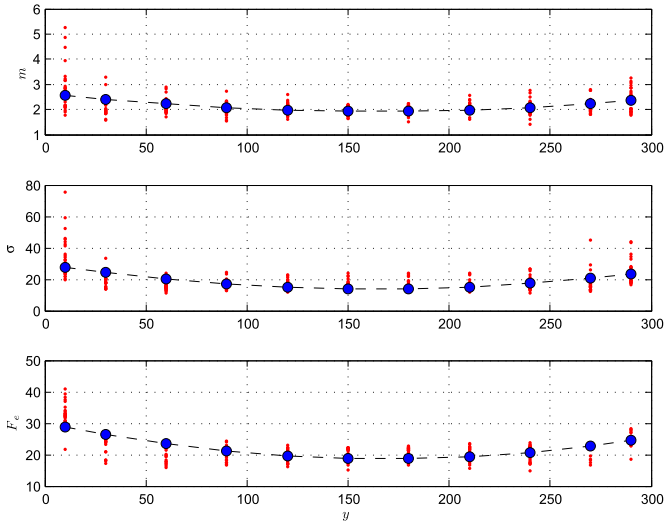

Fig. 7. A typical result from the identified parameter associated to the motions dynamics for 0 kg in red (output from block 4 of Fig. 4), and in blue the fitted polynomial is presented (output from block 5 of Fig. 4). m is in kg, σ is in Ns/mm, F_e is in N and y is in mm. (For interpretation of the references to color in this figure caption, the reader is referred to the web version of this paper.)

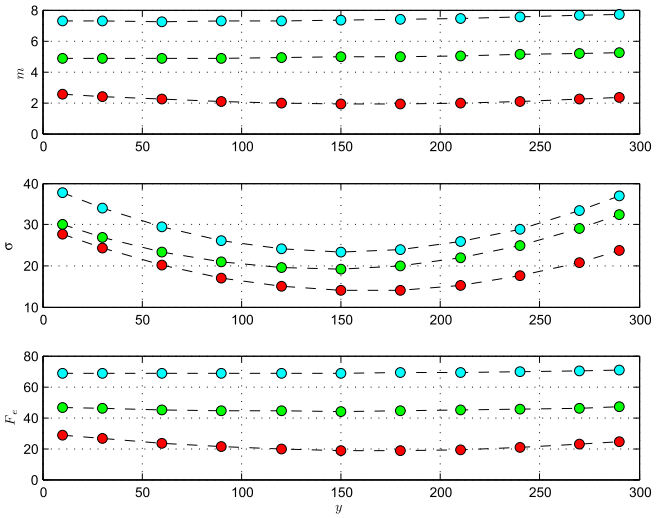

Fig. 8. Parameters of the system for 0 kg (red), 3 kg (green) and 6 kg (cyan). (For interpretation of the references to color in this figure caption, the reader is referred to the web version of this paper.)

observed, the response presents overshooting and decaying oscillations which were intentionally looked for during the selection of the proportional gain of the controller in order to get all the dynamics as possible without falling into instability.

For each register more than 25 identified sets of parameters associated to the transient response of the cylinder motion dynamics were found. A typical result from a single register from an experiment with an external load of 0 kg is presented in Fig. 7. As it can be observed, variability exists on the identified parameters (dots in red). However, a global behavior for m, σ and F_e can also be observed: a minimum value is found at mid position and they increase while moving towards the extreme positions (0 mm and 300 mm). While evaluating several fitting criteria it was found that the identified parameters are best fitted to a quadratic polynomial (dots in blue).

From the fitted curves, it can be observed that the minimum value for the mass is ≈ 2 kg, which corresponds to the mass of the rod, the fluid mass inside the chamber and the coupling elements between the rod and the sliding unit of the test-bed. On the other hand, the mass varies from 2 kg to 2.7 kg, which is in line with the current mass displacement inside the chamber of the cylinder.

It is also possible to appreciate the linear relation between the total mass and the external perturbation. This is caused by the effect of gravity (g) since the experimentation is performed against it, thus the external perturbation is basically given by $F_e \approx mg$.

After all the data is processed, and the identified parameters from the transient response are fitted with a quadratic polynomial, the parameters that govern the dynamics of the system are found (see Fig. 8). As it was expected, the parameters vary with the external. The linear relationship between the mass and the external perturbation is maintained. It can also be seen that the fitted polynomial smoothes while increasing the external load.

From the input–output data (i.e. x_v and y), a close-loop transfer function $G_{cl}(s)$ is found for every transient response, and the open loop transfers functions $G_{ol}(s)$ are obtained from (32).

In Fig. 9, the pole-zero diagram of all the open loop transfers function for an external load of 0 kg is presented. In this picture, it can be observed that the identified models are conformed by a polynomial of fifth-order in the denominator and a fourth-order in the numerator. The increase of the order of the polynomial while the ARMAX structure is estimating is typical when the system to be identified posses a pole near the origin. However, it can be seen that there exist zeros and poles that are very close, thus they can be cancelled. In the same way, the poles and zeros that are located away from the dominant dynamics (see Fig. 9(b)) of the system can also be neglected. It is also observed that the identified models do not have poles exactly at the origin, instead they are very close to it. Therefore, this inaccuracy is neglected and the poles are forced to be at the origin.

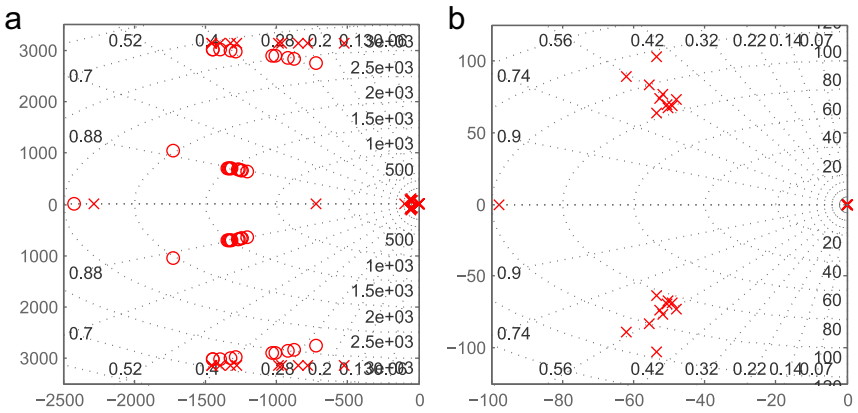

Fig. 9. G_{ol} pole-zero diagram. (a) Complete model (output from *block* 7 of Fig. 4). (b) Governing dynamics (output from *block* 8 of Fig. 4).

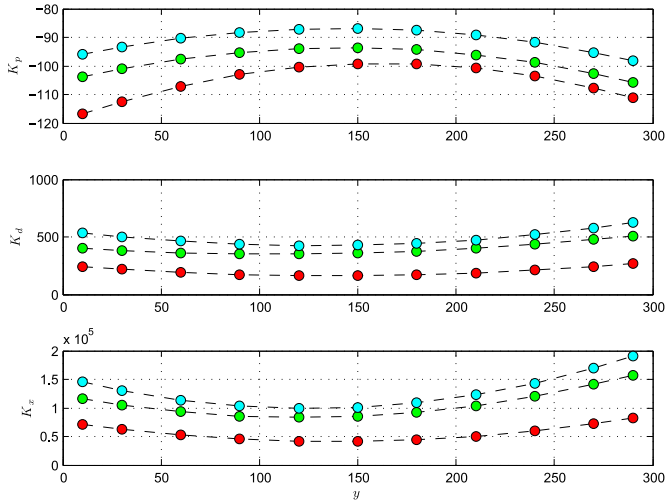

Fig. 10. Identified sensibility constants. 0 kg (red), 3 kg (green) and 6 kg (cyan) of external load (output from *block* 9 of Fig. 4). (For interpretation of the references to color in this figure caption, the reader is referred to the web version of this paper.)

The sensibility constants K_d, K_p and K_x are first approached using the parameters $\tilde{m}$, $\tilde{\sigma}$, $\tilde{F}_e$ (output from *block* 5 of Fig. 4) and the transfer function $G(s)$ (output from *block* 8 of Fig. 4). Then, they are modified in order to maximize (39) using the input–output data from the experiment and the complete linearized model (38). The improved sensibility constants are presented in Fig. 10. As it can be observed, they depend both on the piston's position and the external load, and they present a quadratic behavior.

The complete linearized model is obtained from the parameters identified, and the pole-zero diagram of $P(s) = \Delta Y/\Delta X_v$ is presented in Fig. 11(a). As it can be seen, the systems present the typical pair of conjugate complex poles with a pole at the origin. It can be observed that the location of the complex pair varies with the external load. Furthermore, the complex pair tends to be the origin as the external load increases. As it was expected, the location of the complex pair also varies with the piston's position (see Fig. 11(b)). The localization of the poles gets nearer to the imaginary axis when the piston approaches to its mid stroke position (Watton, 1989). The location of the complex pair varies inside the interval $[-65, -45]\ s^{-1}$ for the real part, and $[75, 125]\ s^{-1}$ for the imaginary part.

All the identified systems are validated by analyzing the capability to reproduce the experimental input–output data. In order to quantify objectively this capability it was used (39). According to this indicator the identified systems provide a range of [85%, 94%] of replicability, which is considered acceptable for the purpose of this work. Furthermore, as it can be observed in Fig. 12 the time response of the identified model and the experimental output data follow the same trends.

The identified parameters are presented in the Appendix.

4. PI controller for the HSA

Recalling, the linearized model of the HSA is given by

$$Y(s) = \frac{k_1 b_0}{s(s^2 + b_1 s + b_0)} X_v(s) - \frac{k_2 b_0 (s + z_0)}{s(s^2 + b_1 s + b_0)} F_e(s), \tag{40}$$

where the controlled variable is the position $Y(s)$ and the manipulated variable is the input current of the servo-valve $X_v(s)$. $F_e(s)$ represents the effects of external forces, which in the absence of external perturbations are mainly due to the action of gravity. Without losing generality for the following analysis, the system is simplified to

$$Y(s) = \frac{k_1 b_0}{s(s^2 + b_1 s + b_0)} X_v(s). \tag{41}$$

Considering the parameters of the identified models, classic P, PI, PD, PID are tuned by simulation and implemented in the real model for control position. The position time responses of the HSA with these controllers are presented in Fig. 13.

These curves show some revealing results:

- P controller does not provide zero steady estate error. For this purpose, a PI controller must be implemented instead.
- PD and PID controllers provide a noisy time response, which is unacceptable for position tracking purposes.

From (41) it is seen that the system has a pole at the origin, therefore it is expected that a simple P controller would be enough in order to provide zero steady state error. However, it can be appreciated in Fig. 13 (red curve) that this is not the case in the real system.

This can be explained by considering once again the complete model, and closing the loop as presented in Fig. 14.

The error $E(s)$ of the system can be found by simple observation and it is given by

$$E = \frac{1}{1 + K_p G_1} Y_R - \frac{G_2}{1 + K_p G_1} F_E. \tag{42}$$

From this expression it can be observed that F_E affects directly to

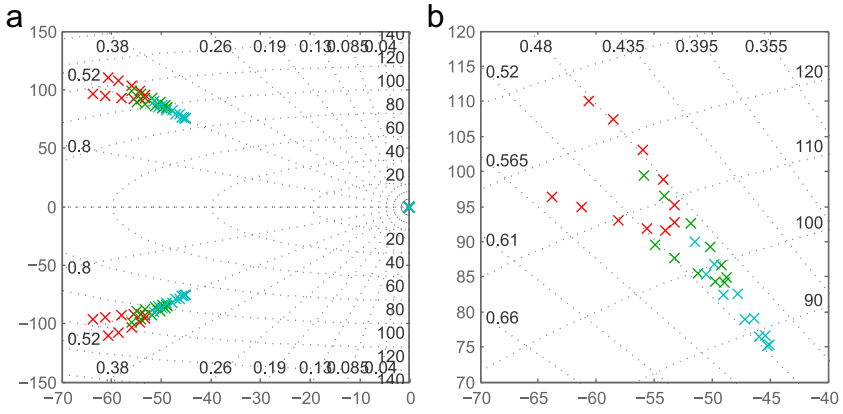

Fig. 11. Pole-zero diagram of $P(s) = \Delta Y/\Delta X$ (output from *block* 11 of Fig. 4). (a) Complete model. (b) Detail of the behavior of the complex pair. 0 kg (red), 3 kg (green) and 6 kg (cyan) of external load. (For interpretation of the references to color in this figure caption, the reader is referred to the web version of this paper.)

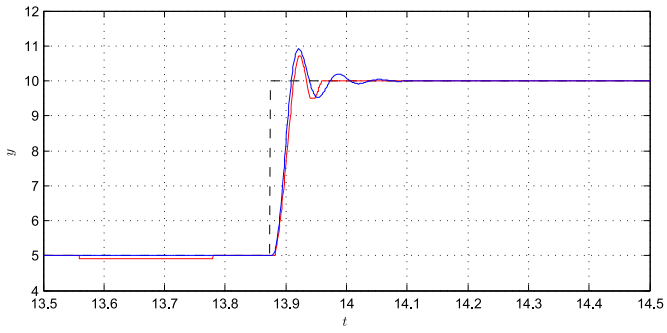

Fig. 12. Simulated response of the identified model. In dashed black is the *PRMS* signal, in red the real output data and in blue the simulated response of the identified model (output from *block* 12 of Fig. 4). (For interpretation of the references to color in this figure caption, the reader is referred to the web version of this paper.)

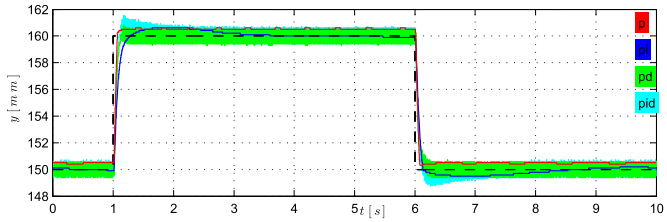

Fig. 13. Time response of the HSA with classic controller for position control. (For interpretation of the references to color in this figure caption, the reader is referred to the web version of this paper.)

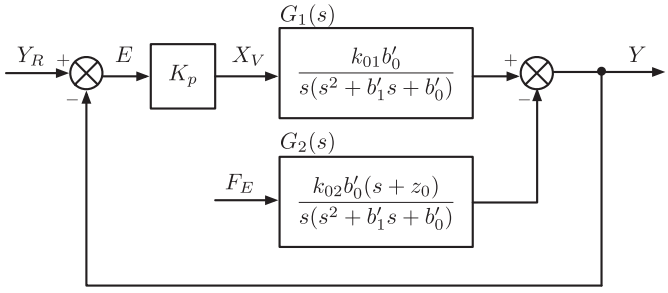

Fig. 14. Steady state analysis block diagram.

the error. Even more, assuming that the reference input is zero (i.e. $Y_R = 0$), and considering the external perturbation as an unitary step, the steady state error e_{ss} will be given by

$$\begin{aligned} e_{ss} &= \lim_{t\to\infty} e(t), \\ &= \lim_{s\to 0} sE(s)|_{Y_R=0}, \\ &= \lim_{s\to 0} s\frac{k_{02}b_0'(s+z_0)}{s^3+b_1's^2+b_0's+K_pk_{01}b_0'}\frac{1}{s}, \\ &= \frac{k_{02}z_0}{K_pk_{01}}, \end{aligned} \tag{43}$$

where $E(s) = \mathcal{L}\{e(t)\}$, and K_p is the gain of the proportional controller. Thus, despite the fact that the model posses a pole at the origin, a proportional controller does not provide zero steady state error, unless K_p is very high which is prohibitive for systems with complex conjugate poles.

Considering now a PI controller of the canonical form $K(s) = K_p + K_i/s$ the steady state error will be given by

$$\begin{aligned} e_{ss} &= \lim_{t\to\infty} e(t), \\ &= \lim_{s\to 0} sE(s)|_{Y_R=0}, \\ &= \lim_{s\to 0} s\frac{k_{02}b_0'(s+z_0)}{s^4+b_1's^3+b_0's^2+K_pk_{01}b_0's+K_ik_1b_0'}\frac{1}{s}, \\ &= 0. \end{aligned} \tag{44}$$

This analytical result can also be observed in Fig. 13, where it is appreciated that the time response reaches the reference value approximately in $t = 4[s]$ (blue curve). However, the implementation of a PI controller with a first type system is controversial, since it will add another pole to the origin in the complex plane, thus reducing drastically the phase margin causing stability issues. Therefore the integrator time constant must be carefully selected. Despite this fact, the use of PI controller is implemented in order to increase the open loop gain at low frequencies and to decrease the steady state error (Jelali & Kroll, 2002).

The stability of the system with a PI controller is analyzed in the next section, where it is proved that the HSA is robust if a suitable PI controller is implemented.

The noisy time response of the system with PD and PID controller can be explained by analyzing the *well-possedness* of the system (Zhou & Doyle, 1999).

Therefore, considering the system rearranged as the standard feedback system presented in Fig. 15, where K is the controller, and G_1 and G_2 are the transfer functions of the linearized model, r is the command or reference signal, f_e is the external force perturbation, n is the sensor noise, d_i is the disturbance at the plant input, and d is the plant output disturbance.

According to *Definition* 5.1 which is related to the performance specification and limitations of feedback systems in Zhou and Doyle (1999):

"*a feedback system is said to be well-posed if all closed-loop transfer matrices are well-defined and proper.*" (As it will be described later a *well posed* system is a physical realizable system).

Therefore, after a few algebraic manipulation it can be found that the closed loop is given by

$$u = \frac{K}{1+KG_1}(r-n-d) - \frac{KG_1}{1+KG_1}d_i + \frac{KG_2}{1+KG_1}f_e. \tag{45}$$

Considering classic P, PI, PD, PID controllers, all the transfer matrices in (45) are obtained. The results for $K/(1+KG_1)$ for all the controllers are presented in Table 1.

As it can be observed, PD and PID controllers do not provide a *well-posed* feedback system, since $K/(1+KG_1)$ is not proper (i.e. the order of the polynomial of the numerator is greater than the order of the polynomial of the denominator). Therefore, PD and PID controllers are prone to noisy outputs as it was found experimentally and shown in Fig. 13 (green and cyan curve respectively), which is in line with Cheng and De Moor (1994) where it was observed that classic PID control design cannot guarantee the stability for a hydraulic servo-system.

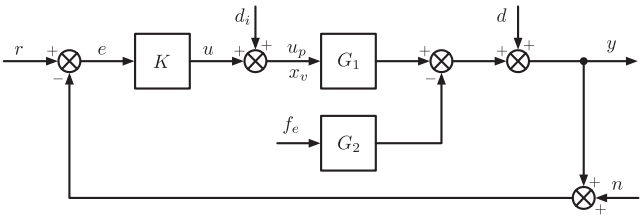

Fig. 15. Schematic diagram for a generic internal stability analysis.

Table 1
Controllers and *well-posedness* of the feedback system.

K	$\frac{K}{1+KG_1}$
P	$\frac{K_p(s^3+b_1s^2+b_0s)}{s^3+b_1s^2+b_0s+K_pk_1b_0}$
PI	$\frac{(K_ps+K_i)(s^3+b_1s^2+b_0s)}{s^4+b_1s^3+b_0s^2+K_pk_1b_0s+K_ik_1b_0}$
PD	$\frac{(K_p+K_ds)(s^3+b_1s^2+b_0s)}{s^3+b_1s^2+(b_0+K_dk_1b_0)s+K_pk_1b_0}$
PID	$\frac{(K_ds^2+K_ps+K_i)(s^3+b_1s^2+b_0s)}{s^4+b_1s^3+(b_0+K_dk_1b_0)s^2+K_pk_1b_0s+k_ik_1b_0}$

4.1. PI controller with robust stability

The main concern of implementing a PI controller for a third-order system with an integrator is whether this controller can provide stability to the system or not.

The HSA system was identified for 33 different set-points resulting in 33 sets of parameters that define the dynamics of the system, which can be expressed as

$$Y = \frac{K_1(y,m)B_0(y,m))}{s(s^2+B_1(y,m)s+B_0(y,m))}X_v - \frac{K_2(y,m)B_0(y,m))(s+Z_0(y,m))}{s(s^2+B_1(y,m)s+B_0(y,m))}F_e. \quad (46)$$

This variability on the parameters remarks the parametric uncertainty of the model.

For the following analysis $G_1(s) = Y(s)/X_v(s)$ is defined as the plant, and the transfer matrix $G_2(s) = Y(s)/F_e(s)$ related with the external perturbation will be incorporated only for the analysis of robustness of the system.

Thus, without losing generality, (46) can be thought as

1. A system whose parameters *move* from a nominal values through a bounded set

$$Y(s) = \frac{k_{10}(1+\delta_k)}{s(s^2+b_{10}(1+\delta_1)s+b_{00}(1+\delta_0))}X_v(s), \quad (47)$$

where $\delta_k \le |\delta_{k_{max}}|$, $\delta_1 \le |\delta_{1_{max}}|$, $\delta_0 \le |\delta_{0_{max}}|$, and k_{10}, b_{10} and b_{00} correspond to the parameters of the nominal system. This formulation, which leads to a *structured uncertainties* definition, presents a more elegant definition of the problem, since the uncertainties can be associated to individual aspects of the physics phenomenon of the system.

2. A system bounded by some weighting functions that characterizes the spatial and frequency structure of the uncertainty $\Delta(s)$. One of the many canonical formulations is the well known *multiplicative uncertainty definition*:

$$\Pi(s) = (1 + W_1(s)\Delta(s)W_2(s))P_0, \quad (48)$$

where $P_0(s)$ is the nominal plant, $W_1(s)$ and $W_2(s)$ are stable transfer matrices, and $\| \Delta \| \le 1$. This particular representation of the set of plants confines $\Pi(s)$ to a normalized neighborhood of the nominal model $P_0(s)$. This type of formulation, known as *unstructured uncertainties* definition, presents the problem as a bounding problem, which does not require much knowledge of the system and may lead to conservative solutions. However, this formulation is much simpler.

In any case, both formulations require the definition of a nominal plant.

4.1.1. Nominal plant definition

In this work, the nominal plant is defined as the identified plant that maximizes (49) for all the input–output data collected during the experimental identification

$$\max_{\forall G_1(s)} \sum_{i=1}^{33} \| F_i \|, \quad (49)$$

where

$$F_i = \frac{1 - \| y_{s_i} - y_i \|}{\| y_i - \bar{y}_i \|}, \quad (50)$$

where y_{s_i} is the simulated output of $G_1(s)$ with the ith input register, y_i is the ith output register, and $\bar{y}_i$ is its mean.

According to this criterion, the nominal plant corresponds to plan identified for the working point [6 kg, 120 mm]:

$$P_0(s) = P_{6\,\mathrm{kg},120\,\mathrm{mm}}(s), \quad (51)$$

$$P_0(s) = \frac{1.722 \times 10^6}{s^3 + 90.31s^2 + 7692s}. \quad (52)$$

4.1.2. Unstructured uncertainty definition

As it was introduced in (48), the system is bounded on the frequency domain by weightings transfer function. Therefore, in order to obtain the unstructured uncertainty bound for this system, first it must be found the discrepancy between the set of plants and the nominal plant, as follows:

$$W_1(s)\Delta(s)W_2 = \frac{\Pi(s) - P_0(s)}{P_0(s)}. \quad (53)$$

Considering a frequency range of $w \in [10^{-2}, 10^3]$, an error plot is generated and presented in Fig. 16.

From this plot (using the *ginput* command of Matlab®) a set of upper-bound frequency response is selected (beyond the maximum errors found presented in dashed red curve) and it is fitted to a stable and minimum phase third-order transfer function (black curve) which represents the bounding weighting transfer function $W_1(s)\Delta(s)W_2(s)$.

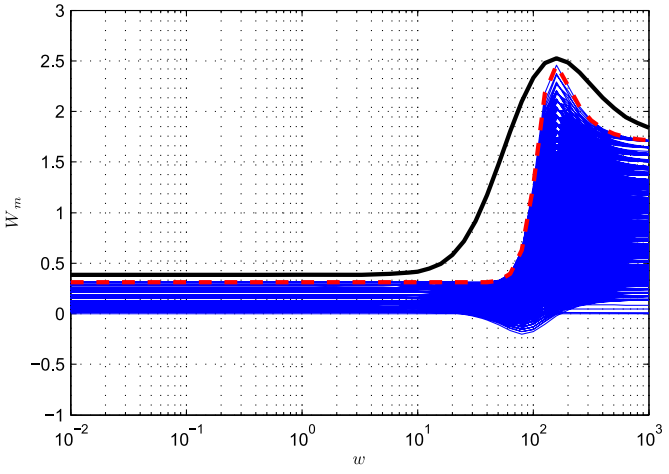

Fig. 16. Multiplicative uncertainty definition. Blue: error plot. Red: maximum error. Black: multiplicative uncertainty weighting transfer function. (For interpretation of the references to color in this figure caption, the reader is referred to the web version of this paper.)

In order to simplify the analysis it is considered that $W_2(s) = 1$, therefore the weighting function $W_1(s)$ is given by

$$W_1(s) = \frac{1.759s^3 + 724.9s^2 + 2.159 \times 10^6 s + 2.406 \times 10^5}{s^3 + 313.9s^2 + 2.65 \times 10^4 s + 6.275 \times 10^5}. \quad (54)$$

4.2. Controller

The controller implemented for the HSA is a classical PI of the form: $K(s) = K_p + K_i/s$. The PI controller is tuned using the classical Ziegler–Nichols (ZN) rules for frequency response (Ziegler & Nichols, 1942).

ZN tuning rules are based on a *two parameter characterization* of the systems dynamic. These parameters represent a very small piece of information of all the system behavior, thus the resulting controller provides a poorly damped response with poor stability margins (Åström & Hägglund, 2004; Hang, Astrom, & Ho, 1991; Hägglund & Åström, 2008). Currently more specific rules exist (O'Dwyer, 2006), and better approaches patented and implemented in commercial software (Yung & Chong, 2006), though for the purpose of this work the ZN provides a kind of suitable harsh scenario for the stability analysis presented in the following sections.

The resulting parameter for the controller is $K_p = 0.085$ and $K_i = 0.46$.

4.3. Robustness analysis

4.3.1. Internal stability (nominal stability)

Internal stability guarantees that all signals in a system are bounded provided that the injected signal at any location is bounded (Zhou & Doyle, 1999).

Definition 1. The system of Fig. 17 is said to be *internally stable* if the transfer matrix

$$\begin{bmatrix} I & -\hat{K} \\ -P & I \end{bmatrix}^{-1} = \begin{bmatrix} (I - \hat{K}P)^{-1} & \hat{K}(I - P\hat{K})^{-1} \\ P(I - \hat{K}P)^{-1} & (I - P\hat{K})^{-1} \end{bmatrix}, \quad = \begin{bmatrix} I + \hat{K}(I - P\hat{K})^{-1}P & \hat{K}(I - P\hat{K})^{-1} \\ (I - P\hat{K})^{-1}P & (I - P\hat{K})^{-1} \end{bmatrix} \quad (55)$$

from (w_1, w_2) to $(e_1, e_2) \in \mathcal{RH}_\infty$, where $P = P_0$ for simplification and $\hat{K} = -K$ (Zhou & Doyle, 1999).

The four transfer matrices presented in the right side of (55) must belong to $\mathcal{RH}_\infty$, i.e. all the poles of the transfer matrices are in $\mathbb{C}^-$.

Arranging the linear feedback system under analysis as the canonical form presented in Fig. 17, it can be found that

$$(I - \hat{K}P)^{-1} = \frac{s^2(s^2 + b_1 s + b_0)}{s^4 + b_1 s^3 + b_0 s^2 + K_p k_1 b_0 s + K_i k_1 b_0} \quad (56)$$

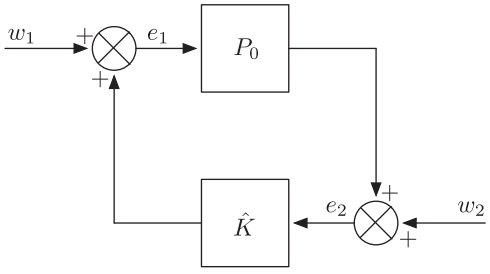

Fig. 17. Schematic diagram for internal stability analysis.

$$P(I - \hat{K}P)^{-1} = \frac{sk_1 b_0}{s^4 + b_1 s^3 + b_0 s^2 + K_p k_1 b_0 s + K_i k_1 b_0} \quad (57)$$

$$\hat{K}(I - P\hat{K})^{-1} = \frac{sk_1 b_0}{s^4 + b_1 s^3 + b_0 s^2 + K_p k_1 b_0 s + K_i k_1 b_0} \quad (58)$$

$$(I - P\hat{K})^{-1} = \frac{s^2(s^2 + b_1 s + b_0)}{s^4 + b_1 s^3 + b_0 s^2 + K_p k_1 b_0 s + K_i k_1 b_0} \quad (59)$$

As it can be observed, the denominators in all transfer functions are the same, and so are their poles. Consequently, replacing the parameters with their corresponding values it is found that the poles are

$$p_{1,2} = -33.3028 \pm 70.4713i$$
$$p_3 = -20.0222$$
$$p_4 = -3.3723 \quad (60)$$

Since all the poles belong to $\mathbb{C}^-$, the system presented in Fig. 17 is internally stable.

4.3.2. Robust stability

In Fig. 18 the Nyquist diagram of $\Pi(s)$ is presented, where the multiplicative uncertainty (depicted as blue circles) clearly dilates the trace of the nominal plant P_0 (red curve). This typical diagram remarks that the controller $K(s)$ must be designed in order to provide stability not only to the nominal plant but also to the family of plant $\Pi(s) = P_0(s)(1 + W_1(s)\Delta(s))$.

The basis for the robust stability criteria is the *Small Gain Theorem* (Zhou & Doyle, 1999), and the Robust Stability of a system can be proved by applying one of the many theorems derived from it. In particular, the Theorem 8.5 from Zhou and Doyle (1999), quoted below, is suitable for this example.

Theorem 1. *Let* Π: $\{(I + W_1\Delta)P_0: \Delta \in \mathcal{RH}_\infty\}$ *and let* K *be a stabilizing controller for the nominal plant* P_0. *Then the closed loop system is well-posed and internally stable for all* $\Delta \in \mathcal{RH}_\infty$ *with* $\|\Delta\|_\infty < 1$ *if and only if* $\|W_1 T_0\|_\infty \leq 1$.

Therefore, after some algebraic manipulation the feedback system with the unstructured multiplicative uncertainty presented

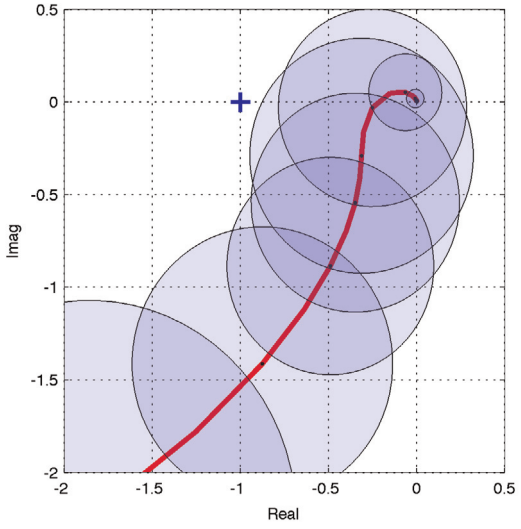

Fig. 18. Nyquist diagram for $\Pi(s)$. Nominal plant in red. Uncertainty in blue disks. (For interpretation of the references to color in this figure caption, the reader is referred to the web version of this paper.) (For interpretation of the references to color in this figure caption, the reader is referred to the web version of this paper.)

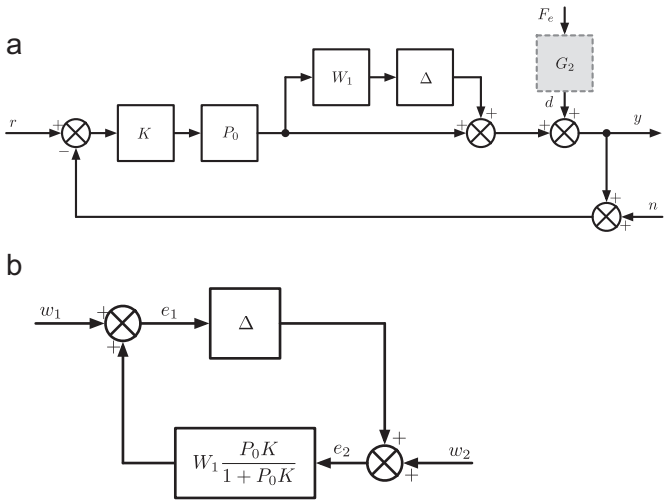

Fig. 19. Multiplicative perturbed system. (a) Linear feedback system. (b) $M-\Delta$ loop arrangement.

in Fig. 19(a) can be structured as the canonical $M-\Delta$ loop as presented in Fig. 19(b), and Theorem 1 can be applied.

By definition $\Delta \in \mathcal{RH}_\infty$ and $\|\Delta\|_\infty < 1$. In the previous section it was proved that K stabilizes the nominal plant P_0, therefore only remains to prove that $\|W_1T_o\|_\infty \le 1$. It must be recalled that $T_o = (P_0K)(1+P_0K)^{-1}$, thus the latter condition can be easily proved by replacing the values P_0 and K and obtaining the infinite norm, which results in

$$\|W_1(jw)T_o(jw)\|_\infty = \left\| W_1(jw)\frac{P_0(jw)K(jw)}{1+P_0(jw)K(jw)} \right\|_\infty = 0.8523 \le 1. \quad (61)$$

Then, the system is internally stable.

4.3.3. Robust performance

In this work the robust performance of the system is analyzed in terms of how the external perturbation affects the output. More precisely, the performance criterion adopted is to keep the worst-case energy of the output as small as possible over a unit energy input $\tilde{d}$.

The defined robust performance criterion is satisfied if and only if (Zhou & Doyle, 1999)

$$\|W_1T_o\|_\infty \le 1, \quad (62)$$

$$\|T_{y\tilde{d}}\|_\infty \le 1, \quad \forall\, \Delta \in \mathcal{RH}_\infty, \ \|\Delta_d\|_\infty \le 1\}. \quad (63)$$

These two bounding inequalities give sufficient conditions for the robust performance problem.

The first bounding inequality was already proved above. Therefore, the second inequality remains to be proved.

Let us consider the general perturbed feedback system presented in Fig. 19(a). As it was mentioned previously G_2 is associated with the action of external forces, and it could be considered as a weighting matrix function for the external perturbation.

As it was presented in Section 2.1, the parameters of this transfer function are variable according to the current set-point, thus G_2 is a set of transfer functions, which for simplicity it will be defined as the bounded set: Ω: $\{(1+W_{dm}\Delta_d)W_0$: W_{dm}, W_0, $\Delta_d \in \mathcal{RH}_\infty$, $\|\Delta_d\|_\infty \le 1\}$. This kind of multiplicative unstructured definition for the set of weighting functions provides a better approach to the formulation of the problem. Where W_0 is the *nominal* weighting function and W_{dm} is the *multiplicative* bounding weight.

The nominal weighting function is defined with the parameters used in P_0, then

$$W_0(s) = \frac{0.1372s + 11.93}{s^3 + 90.31s^2 + 7692s}. \quad (64)$$

The multiplicative weighting function W_{dm} is found using the same procedure for the definition of W_1, and it results in

$$W_{dm}(s) = \frac{2.951s^3 + 781.4s^2 + 2.66\times10^4 s + 5342}{s^3 + 240.6s^2 + 1.319\times10^4 s + 2695}. \quad (65)$$

Considering these elements, it is found by simple observation of Fig. 19(a) that

$$T_{y\tilde{d}} = (1+K\Pi)^{-1}\Omega \quad (66)$$

$$=[1+(1+W_1\Delta)]^{-1}(1+W_{dm}\Delta_d)W_0. \quad (67)$$

and its infinite norm is given by

$$\|T_{y\tilde{d}}\|_\infty = 2.1434\times10^{-4} \le 1. \quad (68)$$

Therefore, since $\|W_1T_o\|_\infty \le 1$ and $\|T_{y\tilde{d}}\|_\infty \le 1$, then the system presents robust performance for bounded external perturbation.

5. Experiments

The following section presents a series of experiments that allows an analysis of the performance of the PI controller.

In the first two experiments it is expected that the responses of the controlled system keep the same overshoot, settling time and tracking error within a range of 10% of variation for all the position and external forces. In the third experiment it is expected that the action of an external force does not lead to instability.

5.1. Experiment # 1: step response

Objective: To analyze the characteristics of time response of the system in closed loop for different set points.

Description: The HSA is submitted to step inputs of 10 mm of amplitude in closed loop implementing the PI controller, driving external loads of m_{ext}:={0, 3, 6} kg, and working position, y_0:={50, 150, 250} mm.

Data processing: All the curves obtained during experimentation are synchronized with the step input and it eliminated the bias signal.

Results: The time responses with the PI controller are presented in Fig. 20. As it can be observed, the time responses are very similar for all the different set-points, presenting an overshoot of ≈25% with no oscillation and a settling time of 500 ms with a variation below the 5% on all the cases.

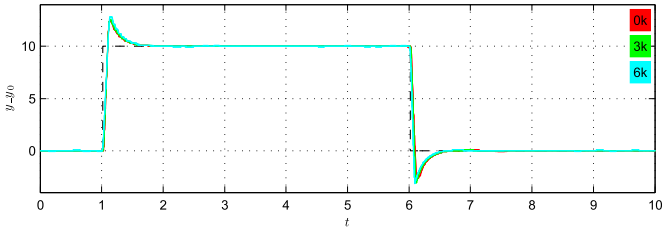

Fig. 20. Step response of the system for different working set points.

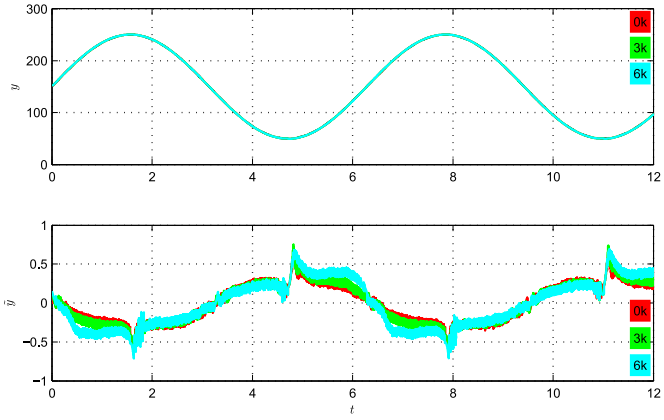

Fig. 21. Reference tracking with PI controller.

5.2. Experiment # 2: position reference tracking

Objective: To analyze the reference tracking capabilities of the controller, by evaluating the error between the command signal and the response of the system, and its frequency dependency.

Description: The controlled system is submitted to follow the trajectory: $y_r(t) = 150 + 125\sin(wt)$ mm, driving external loads of m_{ext}:={0, 3, 6} kg, with frequencies $w \in [0.1, 10]$ rad/s.

Data processing: The signals obtained during experimentation are synchronized with the input signal at the biased position. In order to quantify the dependency of the error in terms of the frequency of the input signal the maximum absolute error for each data set is considered, i.e. $|\tilde{y}(t)|_{max}$.

Results: The response of the system to the desired trajectory $y_r(t)$ using the PI controller driving different external loads is presented in Fig. 21. As it is seen, the controller presents a tracking error $\tilde{y}(t) \leq 1$ mm. It can also be appreciated that the maximum of $\tilde{y}(t)$ corresponds to the change of direction on the piston motion. Even further, an abrupt change in the error can be appreciated that could be associated to stick-slip phenomena between the moving elements.

The dependency of the error to the frequency of the input signal is depicted in Fig. 22. As it was expected, the error increases with the frequency of the signal input.

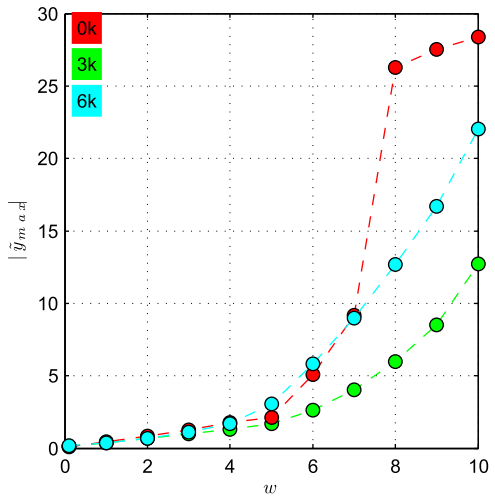

Fig. 22. Frequency error dependency.

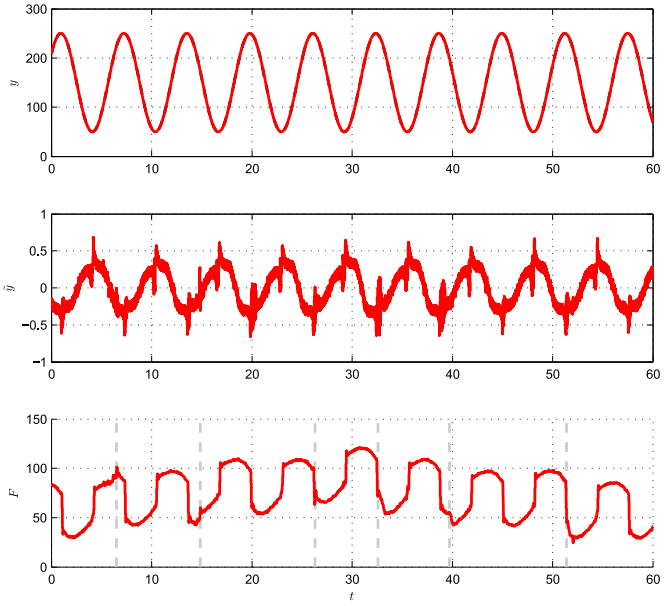

Fig. 23. PI controller response under external perturbations.

5.3. Experiment # 3: robustness to external perturbations

Objective: To demonstrate the robustness of the system in face of external force perturbation.

Description: The actuator is submitted to a sinusoidal input in closed loop. External force perturbation is performed by adding and removing weights during operation.

Results: The time response of the system with PI controller in face of external force perturbation is presented in Fig. 23. In these charts, it is presented the position of the systems $y(t)$, the error tracking $\tilde{y}(t)$ and the measured force $F(t)$. In the latter chart it can be observed the action of the external mass (signaled as dashed grey vertical lines), and how it alters the force system of the HSA. As it can be observed on $y(t)$ and $\tilde{y}(t)$, these perturbations do not present major significance for the output of the system.

6. Conclusions and discussions

In this work, was presented based on the linearization and experimental identification of HSA in order to prove the robustness of the system with a classic PI position controller.

The linearized model of the HSA consists of two parts, one of them is associated with the manipulated variable and the other with the action of external forces. It has been demonstrated in this work that if the model is simplified just to its first part, it is easy to fall into erroneous design of the controller, since the second part is directly coupled to the output affecting the steady state error.

It was also shown that in order to provide zero state error it needed a PI controller, and that PD and PID controllers lead to noisy output. The latter was theoretically demonstrated by analyzing the *well-posedness* of the system, and further proved in the experimentation.

The implementation of a PI controller to the HSA is always controversial, since it adds another integrator in the open-loop system. Therefore, the linearized model was identified for 33 different working points, and the variability between the parameters was considered as the parametric uncertainty of the system. Thus, by implementing a theorem derived from the *Small Gain Theorem* the robustness of the system was proved theoretically. In order to

Table A1
Parameters of motion.

P_o	m_{0k}	σ_{0k}	F_{e0k}	m_{3k}	σ_{3k}	F_{e3k}	m_{6k}	σ_{6k}	F_{e6k}
10	2.57	27.69	28.8	4.87	29.97	46.56	7.28	37.66	68.67
30	2.41	24.31	26.42	4.87	26.97	45.9	7.27	33.93	68.57
60	2.22	20.12	23.44	4.87	23.38	45.1	7.26	29.38	68.49
90	2.08	17	21.19	4.89	20.89	44.55	7.27	26.11	68.49
120	1.98	14.96	19.66	4.92	19.49	44.24	7.29	24.12	68.58
150	1.93	13.99	18.85	4.95	19.2	44.17	7.33	23.4	68.76
180	1.93	14.09	18.77	5	20.01	44.34	7.38	23.96	69.03
210	1.98	15.26	19.41	5.05	21.91	44.76	7.46	25.8	69.38
240	2.08	17.5	20.77	5.12	24.91	45.41	7.54	28.91	69.81
270	2.23	20.82	22.86	5.19	29.02	46.31	7.65	33.29	70.34
290	2.35	23.62	24.66	5.24	32.36	47.04	7.72	36.93	70.74

Table A2
Sensibility constants.

P_o	K_{x0k}	K_{d0k}	K_{p0k}	K_{x3k}	K_{d3k}	K_{p0k}	K_{x6k}	K_{d6k}	K_{p6k}
10	71,690	244	−117	115,886	399	−104	145,261	536	−96
30	62,876	221	−112	105,248	382	−101	130,609	502	−93
60	52,427	193	−107	93,220	363	−98	113,806	462	−90
90	45,303	175	−103	85,909	353	−95	103,211	437	−88
120	41,503	164	−100	83,314	352	−94	98,826	425	−87
150	41,029	163	−99	85,436	360	−94	100,650	428	−87
180	43,880	170	−99	92,273	376	−94	108,683	445	−88
210	50,055	186	−101	103,827	401	−96	122,925	475	−89
240	59,556	211	−104	120,097	435	−99	143,376	520	−92
270	72,382	245	−108	141,084	477	−103	170,037	579	−95
290	82,780	272	−111	157,695	510	−106	191,260	625	−98

Table A3
Parameter of the transfer functions.

P_o	$b_{0_{0k}}$	$b_{1_{0k}}$	$k_{01_{0k}}$	$b_{0_{3k}}$	$b_{1_{3k}}$	$k_{01_{3k}}$	$b_{0_{6k}}$	$b_{1_{6k}}$	$k_{01_{6k}}$
10	13,345	128	266	11040	110	274	9837	101	258
30	12,771	122	259	10515	106	261	9201	98	248
60	12,036	116	249	9929	102	245	8453	94	236
90	11,522	111	241	9583	99	233	7952	92	227
120	11,302	108	236	9471	98	227	7701	90	224
150	11,425	106	236	9591	97	229	7696	90	227
180	11,905	107	242	9936	98	236	7933	91	236
210	12,706	108	252	10,498	100	249	8405	93	249
240	13,754	112	264	11,270	104	265	9106	96	265
270	14,956	117	276	12,243	108	282	10,024	100	282
290	15,799	121	283	13,000	112	294	10,751	103	292

demonstrate this result, the HSA was submitted to tests where its performance was analyzed. From these tests it was found that it is possible to achieve robustness of the system with a PI controller if it is properly designed. The expected 10% criteria adopted for the principal time-response characteristics (overshoot, settling time and tracking error) were met. Though if it were not the case it would have been necessary to apply a better tuning rule than ZN in order to provide less variation among the set-point.

In a future work the robustness of the system in face of the non-linearities not considered in this work will be analyzed. For example a hydraulic pump can deliver a maximum flow therefore the hydraulic actuator can provide a maximum output velocity. This non-linear constraint may explain the limited bandwidth.

Acknowledgments

The authors would like to thank the financial support of the Spanish Government through the CICYT Project Ref. DPI2009-08778 and also to Comunidad de Madrid who supports the project ROBOCITY2030-II Ref. P2009/DPI-1559.

Appendix A. Identified parameters

See Tables A1–A3.

References

Åström, K. J., & Hägglund, T. (2004). Revisiting the Ziegler–Nichols step response method for PID control. *Journal of Process Control*, *14*(September (6)), 635–650.
Bobrow, J. E.; Lum, K., Adaptive, high bandwidth control of a hydraulic actuator, American Control Conference, Proceedings of the 1995, Seattle, WA, Vol.1, pp. 71–75, 1, 21–23 June 1995. http://dx.doi.org/10.1109/ACC.1995.529210.
Chen, Hong-Ming, Renn, Jyh-Chyang, & Su, Juhng-Perng (2005). Sliding mode control with varying boundary layers for an electro-hydraulic position servo system. *The International Journal of Advanced Manufacturing Technology*, *26* (January (1–2)), 117–123.
Cheng, Yi, & De Moor, B. L. R. (1994). Robustness analysis and control system design for a hydraulic servo system. *IEEE Transactions on Control Systems Technology*, *2* (3), 183–197.
Hägglund, T., & Åström, K. J. (2008). Revisiting the Ziegler–Nichols tuning rules for PI control—Part II: The frequency response method. *Asian Journal of Control*, *6* (October (4)), 469–482.
Hang, C. C., Astrom, K. J., & Ho, W. K. (1991). Refinements of the Ziegler–Nichols tuning formula. *Control Theory and Applications, IEE Proceedings D*, *138*(2), 111–118.
Hwang, C.-L. (1996). Sliding mode control using time-varying switching gain and boundary layer for electrohydraulic position and differential pressure control. *IEE Proceedings—Control Theory and Applications*, *143*(4), 325.
Jelali, Mohieddine, & Kroll, Andreas (2002). *Hydraulic servo-systems. Modelling, identification and control series: Advances in industrial control* ((1st ed.). London, Great Britain: Springer.
Jelali, Mohieddine, & Schwarz, Helmut (1995). Nonlinear identification of hydraulic servo-drive systems. *IEEE Control Systems Magazine*, *15*(5), 17–22.
Karpenko, M., & Sepehri, Nariman (2005). Fault–tolerant control of a servohydraulic positioning system with crossport leakage. *IEEE Transactions on Control Systems Technology*, *13*(January (1)), 155–161.
Kim, D. H.; Tsu-Chin Tsao, An improved linearized model for electrohydraulic servovalves and its usage for robust performance control system design, American Control Conference, 1997. Proceedings of the 1997, Albuquerque, NM, Vol. 6, pp. 3807–3808, 6, 4–6 June 1997. http://dx.doi.org/10.1109/ACC.1997.609563.
Kim, D. H. & Tsao, T. -C. (2000). Robust performance control of electrohydraulic actuators for electronic cam motion generation. *IEEE Transactions on Control Systems Technology* (March (2)), 220–227.
La Hera, Pedro, Mettin, Uwe, Manchester, Ian R., & Shiriaev, Anton. (2008). Identification and Control of a Hydraulic Forestry Crane. In Chung Myung (Ed.), *Proceedings of the 17th IFAC World Congress* (pp. 2306–2311), July 2008.
Laval, Laurent, M'Sirdi, N. K., &Cadiou, J.-C. "H/sub /-force control of a hydraulic servo-actuator with environmental uncertainties. In Proceedings of IEEE International Conference on Robotics and Automation, Minneapolis, MN (Vol.2, pp. 1566–1571, 2, 22–28 Apr 1996). http://dx.doi.org/10.1109/ROBOT.1996.506927.
Liao, Hsien-hsin, Roelle, Matthew J., Chen, Jyh-shin, Park, Sungbae, & Gerdes, J. Christian (2011). Implementation and analysis of a repetitive controller for an electro-hydraulic engine valve system. *IEEE Transactions on Control Systems Technology*, *19*(September (5)), 1102–1113.
Ling, T. G.; Rahmat, M. F.; Husain, A. R.; Ghazali, R., System identification of electro-hydraulic actuator servo system, Mechatronics (ICOM), In 2011 4th International Conference On ,Kuala Lumpur, pp. 1,7, 17–19 May 2011. http://dx.doi.org/10.1109/ICOM.2011.5937172.
Liu, G. P., & Daley, S. (1999). Optimal-tuning PID controller design in the frequency domain with application to a rotary hydraulic system. *Control Engineering Practice*, *7*(July (7)), 821–830.
Ljung, Lennart (2002). *System Identification Toolbox User's Guide*. Natick, MA: The Math Works, Inc.
Mohanty, Amit, & Yao, Bin (2011). Integrated direct/indirect adaptive robust control of hydraulic manipulators with valve deadband. *IEEE/ASME Transactions on Mechatronics*, *16*(August (4)), 707–715.
Niksefat, N., & Sepehri, Nariman (2001). Designing robust force control of hydraulic actuators despite system and environmental uncertainties. *IEEE Control Systems Magazine*, *21*(April (2)), 66–77.
O'Dwyer, Aidan (2006). *Handbook of PI and PID controller tuning rules* ((2nd ed.). London: Imperial College Press.
Rahmat, M. F., Rozali, S., Wahab, N. A., Zulfatman, & Kamaruzaman, J. (2010). Modeling and controller design of an electro-hydraulic actuator system. *American Journal of Applied Sciences*, *7*(August (8)), 1100–1108.
Sepehri, Nariman, Corbet, T., & Lawrence, P. D. (1995). Fuzzy position control of hydraulic robots with valve deadbands. *Mechatronics*, *5*(September (6)), 623–643.

Watton, John (1989). *Fluid power systems. Modeling, simulation, analog and microcomputer control*. Upper Saddle River, NJ, USA: Prentice-Hall International Ltd.

Yung, .Li, & Chong, G. C. Y. (2006). Patents, software, and hardware for PID control: *An overview and analysis of the current art*. *IEEE Control Systems Magazine*, *26* (February (1)), 42–54.

Zhao, Tienan, & Virvalo, Tapio (1995). Development of fuzzy state controller and its application to a hydraulic position servo. *Fuzzy Sets and Systems*, *70*(March (2–3)), 213–221.

Zhou, Kemin, & Doyle John, C. (1999). *Essentials of robust control*. Upper Saddle River, NJ, USA: Prentice-Hall.

Ziegler, J. G., & Nichols, N. B. (1942). Optimum settings for automatic controllers. *Transaction of the ASME*, *64*, 759–768.

Zulfatman, & Rahmat, M. F. (2009). Application of self tuning fuzzy PID controller on industrial hydraulic actuator. *International Journal on Smart Sensing and Intelligent Systems*, *2*(2), 246–261.